Mineralogical Magazine (2022), **86**, 777–791
doi:10.1180/mgm.2022.62

CAMBRIDGE UNIVERSITY PRESS

Article

Crystal chemistry and Raman spectroscopy study of bennesherite, $Ba_2Fe^{2+}Si_2O_7$, and rare accessory Ba minerals from Caspar quarry, Bellerberg volcano, Germany

Rafał Juroszek[1]* and Bernd Ternes[2]

[1]Institute of Earth Sciences, Faculty of Natural Sciences, University of Silesia, Będzińska 60, 41-205, Sosnowiec, Poland; and [2]Retired, Mayen, Germany

Abstract

Barium melilite – bennesherite, $Ba_2Fe^{2+}Si_2O_7$, known only from pyrometamorphic rocks of the Hatrurim Complex in Israel, has been recognised in a carbonate–silicate xenolith from the Bellerberg volcano area in Germany. The empirical formula of the German specimen is as follows: $(Ba_{1.32}Ca_{0.43}Sr_{0.23}Na_{0.05}K_{0.02})_{\Sigma 2.05}(Fe^{2+}_{0.79}Ti_{0.06}Mg_{0.05}Al_{0.04}Mn_{0.03}Zn_{0.01})_{\Sigma 0.98}Si_{1.97}O_7$. The Raman spectrum of bennesherite exhibits the presence of the main vibrations related to $Fe^{2+}O_4$ tetrahedra and disilicate Si_2O_7 groups at the T1 and T2 sites, at 589 cm^{-1} and in the range 618–673 cm^{-1}, respectively. Detailed spectroscopic analyses performed for bennesherite in two different and random orientations confirm the reduction of bands intensity and the number of some components in several spectral ranges. Moreover, the presence of a heavy Ba atom indicates a decrease in band frequencies compared to melilites with Ca at the X position. A single-crystal X-ray diffraction experiment, despite attempts, could not be carried out due to the poor quality and small size of the bennesherite crystals however, a combination of composition and Raman data allowed for accurate phase identification. Detailed mineralogical investigations distinguished rare Ba minerals in association with bennesherite, such as walstromite, fresnoite and celsian, along with various ferrous melilites. Some of the detected phases are described from xenoliths of the Bellerberg volcano for the first time. The uniqueness of the Bellerberg volcano mineralisation is reflected in the interaction of alkaline magma with xenoliths of different compositions, which suggests that this locality still deserves attention as a source of new and unique minerals.

Keywords: bennesherite, walstromite, fresnoite, celsian, Raman spectroscopy, Bellerberg volcano, Germany

(Received 21 March 2022; accepted 28 June 2022; Accepted Manuscript published online: 13 July 2022; Associate Editor: Koichi Momma)

Introduction

Bennesherite, $Ba_2Fe^{2+}Si_2O_7$, the only Ba-member of the melilite group, has been recognised in xenolith samples from Caspar quarry, Bellerberg volcano, Germany (50.35°N, 7.23°E). This well-known geological locality, where over a dozen new minerals have now been described, is a part of the quaternary volcanic region in the Eastern Eifel, characterised by the occurrence of different thermally metamorphosed carbonate–silicate and silicate xenoliths within a basaltic, mostly leucite-tephrite lava (Hentschel, 1987; Mihajlovic *et al.*, 2004).

Bennesherite belongs to the melilite group, which contains the other mineral species: åkermanite, $Ca_2MgSi_2O_7$ (Swainson *et al.*, 1992); alumoåkermanite, $(Ca,Na)_2(Al,Mg,Fe^{2+})(Si_2O_7)$ (Wiedenmann *et al.*, 2009); hardystonite, $Ca_2ZnSi_2O_7$ (Wolff, 1899); gugiaite, $Ca_2BeSi_2O_7$ (Peng *et al.*, 1962); hydroxylgugiaite, $(Ca_3\square)_{\Sigma 4}(Si_{3.5}Be_{2.5})_{\Sigma 6}O_{11}(OH)_3$ (Grice *et al.*, 2017); okayamalite; $Ca_2B_2SiO_7$ (Matsubara *et al.*, 1998); and gehlenite, $Ca_2Al(SiAl)O_7$ (Louisnathan, 1971). The general formula of the melilite-group minerals is $X_2T1(T2)_2O_7$, where: X = □ [vacancy], Na, K, Ca, Ba and Sr; T1 = B, Be, Mg, Fe^{2+}, Zn, Fe^{3+}, Al and Si; and T2 = Si, Al, B and Be. All minerals of the melilite group are tetragonal. Their crystal structures consist of $T2_2O_7$ dimers connected with cations at T1 tetrahedra, which form a sheet-like arrangement. These sheets are linked together by large cations coordinated by the eight oxygen atoms at the X site (Bindi *et al.*, 2001). The members of the melilite group usually occur in igneous and metamorphic rocks, however they have also been identified in meteorites and blast-furnace slags (Ardit *et al.*, 2010). Nevertheless, for some characteristic localities such as the Bellerberg volcano, Germany (Galuskin *et al.*, 2016) or the enigmatic Hatrurim Complex in Israel (Galuskin *et al.*, 2015), these phases are rock-forming minerals.

Bennesherite was found recently in the veins of coarse-grained rankinite paralava in pyrometamorphic rocks of the Hatrurim Complex (Gurim Anticline locality, Krzątała *et al.*, 2022). The authors performed a series of investigations, including chemical, structural and spectroscopic analyses of this new mineral, and compared the data with other members of the melilite group. However, the first description and chemical data of the natural $Ba_2Fe^{2+}Si_2O_7$ phase, named barium–iron silicate, came from highly peralkaline leucite nephelinites at the Nyiragongo volcano in the Virunga volcanic province, Democratic Republic of Congo (Andersen *et al.*, 2014). In addition, in Russian-language literature, a synthetic phase named barium ferroåkermanite has been examined using Mössbauer spectroscopy (Bychkov *et al.*, 1992).

*Author for correspondence: Rafał Juroszek, Email: rafal.juroszek@us.edu.pl
Cite this article: Juroszek R. and Ternes B. (2022) Crystal chemistry and Raman spectroscopy study of bennesherite, $Ba_2Fe^{2+}Si_2O_7$, and rare accessory Ba minerals from Caspar quarry, Bellerberg volcano, Germany. *Mineralogical Magazine* **86**, 777–791. https://doi.org/10.1180/mgm.2022.62

The research presents new data confirming the occurrence of the very rare mineral bennesherite. In this paper, we also describe other, potentially new, melilite-group minerals and some unique accessory Ba-bearing minerals such as walstromite, $BaCa_2Si_3O_9$, fresnoite, $Ba_2TiO(Si_2O_7)$ and celsian, $Ba(Al_2Si_2O_8)$ from Caspar quarry xenoliths, which are recognised and investigated from this locality for the first time. The results and detailed analyses presented in this paper are compared and discussed with data reported previously.

Materials and methods

Samples of carbonate–silicate xenoliths were collected from Caspar quarry, Bellerberg volcano in Germany. The rock samples were cut, and thin sections were prepared for analytical investigations.

The preliminary study of the xenoliths, including minerals identification and composition, was using a scanning electron microscope (SEM) Phenom XL equipped with an energy-dispersive X-ray spectroscopy (EDS) detector (Institute of Earth Sciences, Faculty of Natural Sciences, University of Silesia, Sosnowiec, Poland). These semi-quantitative composition measurements were performed using a high vacuum (1 Pa), with a beam voltage of 15 kV and a working distance of 6 mm.

Quantitative analyses of minerals were carried out using a CAMECA SX100 electron-microprobe operating in WDS (wavelength dispersive X-ray spectroscopy) mode (Faculty of Geology, University of Warsaw, Warsaw, Poland) at 15 kV and 10–20 nA with beam size ~1–2 μm. The following X-ray lines (and standards) were used: Na*K*α (albite); Ca*K*α, Si*K*α and Mg*K*α (diopside); K*K*α and Al*K*α (orthoclase); Ti*K*α (rutile); Ba*L*α (baryte); Fe*K*α (Fe_2O_3); Sr*L*α (celestine); Mn*K*α (rhodonite); and Zn*K*α (sphalerite).

The Raman spectra of bennesherite and accessory minerals presented in this paper were recorded on a WITec alpha 300R Confocal Raman Microscope (Institute of Earth Sciences, Faculty of Natural Sciences, University of Silesia, Sosnowiec, Poland) equipped with an air-cooled solid laser of 488 nm and a CCD camera operating at –61°C. The laser radiation was coupled to a microscope through a single-mode optical fibre with a diameter of 3.5 μm. An air Zeiss (LD EC Epiplan-Neofluan DIC–100/0.75NA) objective was used. Raman scattered light was focused by an effective Pinhole size of ~30 μm and a monochromator with a 600 mm^{-1} grating. The power of the laser at the sample position was 42 mW. Integration times of 5 s with an accumulation of 20 scans were chosen and a resolution of 3 cm^{-1}. The monochromator was calibrated using the Raman scattering line of a silicon plate (520.7 cm^{-1}). Spectra processing was performed using the Spectracalc software package *GRAMS* (Galactic Industries Corp, USA). The Raman bands were fitted using a Gauss–Lorentz cross-product function with the minimum number of component bands used for the fitting process.

Results and discussion

Mineral composition of the xenoliths

The SEM investigations revealed that some of the thermally metamorphosed carbonate–silicate xenoliths contain secondary alteration, and that low-temperature mineral assemblages prevail over the rock-forming minerals. The primarily high-temperature constituents of the altered xenoliths are larnite, gehlenite and magnesioferrite. Bredigite, kalsilite, chlormayenite, fluorapatite, srebrodolskite and members of the shulamitite–sharyginite series occur as accessory minerals. Some Zr-phases, such as lakargiite, baddeleyite, calzirtite and zircon, were also noted. Hematite, pyrite and an unidentified Y–Fe–Al oxide occur very rarely. The abundance of secondary phases is represented by different hydrated Ca-silicates and aluminosilicates such as tobermorite, jennite, afwillite, hydrocalumite, calcite, baryte, Sr-bearing baryte, minerals of the ettringite–thaumasite series and Sr-rich thomsonite-Ca.

The non-altered xenolith fragments are composed of wollastonite, nepheline and minerals of the melilite group, represented mainly by alumoåkermanite and Fe^{2+}-rich åkermanite. The composition of the melilite-group minerals is variable and in some cases they are enriched in Na, Ba and Sr. Perovskite, rare Ba-minerals such as bennesherite, walstromite, fresnoite, celsian, zadovite and a P-analogue of gurimite, as well as wadeite, are accessory phases. Some of these accessory minerals are recognised for the first time in this locality.

Occurrence, chemical composition and Raman spectroscopy

Bennesherite from the carbonate–silicate xenoliths formed subhedral crystals up to 30 μm in size and was detected within large wollastonite crystals in non-altered parts/zones of the xenolith (Fig. 1a). In addition to the wollastonite, the melilite-group mineral, alumoåkermanite, is associated with bennesherite (Fig. 1a,b). It is noteworthy that a small ~10–12 μm inclusion of the potentially new mineral, a P-analogue of gurimite, $Ba_3(PO_4)_2$, was found in a bennesherite crystal (Fig. 1b). Under transmitted light, the bennesherite crystals are transparent and exhibit a bright yellow colour (Fig. 1c). The same optical properties were determined for the Israeli specimen, however, as reported for some Israeli crystals, bennesherite from Germany does not show low-temperature changes, such as partial substitution by hydrosilicates on the crystal edges (Krzątała *et al.*, 2022).

The analytical data for bennesherite from Caspar quarry, Bellerberg volcano, Gurim Anticline, Hatrurim Complex (holotype locality), and Nyiragongo volcano localities are presented in Table 1. The empirical formula of bennesherite from Caspar quarry calculated on the basis of 7 O atoms per formula unit (apfu) is: $(Ba_{1.32}Ca_{0.43}Sr_{0.23}Na_{0.05}K_{0.02})_{\Sigma 2.05}(Fe^{2+}_{0.79}Ti_{0.06}Mg_{0.05}Al_{0.04}Mn_{0.03}Zn_{0.01})_{\Sigma 0.98}Si_{1.97}O_7$, which can be simplified to the end-member formula $Ba_2Fe^{2+}Si_2O_7$. This mineral is represented by a complex solid solution containing the following end-members: ~68% bennesherite, ~12% Sr-analogue of bennesherite and ~12% åkermanite-like members (åkermanite, Fe^{2+}-åkermanite and Mn-åkermanite). The remaining 10% comes from other components. The composition of the studied bennesherite differs in Ba, Ca and Sr contents compared to specimens from the other two localities (Table 1). Partial or complete isomorphic substitution of Ca, at the polyhedral X position, by Sr and Ba is a common phenomenon, which has been observed in synthetic analogues and some natural melilites (Kimata, 1983, 1984; Bindi *et al.*, 2001; Ardit *et al.*, 2012; Krzątała *et al.*, 2022). However, bennesherite is the first mineral in which an element other than Ca prevails on the X structural position. The higher Ba content in the Israeli holotype sample indicates that the bennesherite end-member contribution of ~83% is more significant than other end-members (Table 1). Specimens from Germany and DRC (the Democratic Republic of the Congo) contain more Sr than the Israeli holotype (Table 1), both with 12% of the Sr-dominant end-member, $Sr_2FeSi_2O_7$. Considering the tetrahedral positions, we assumed that

https://doi.org/10.1180/mgm.2022.62 Published online by Cambridge University Press

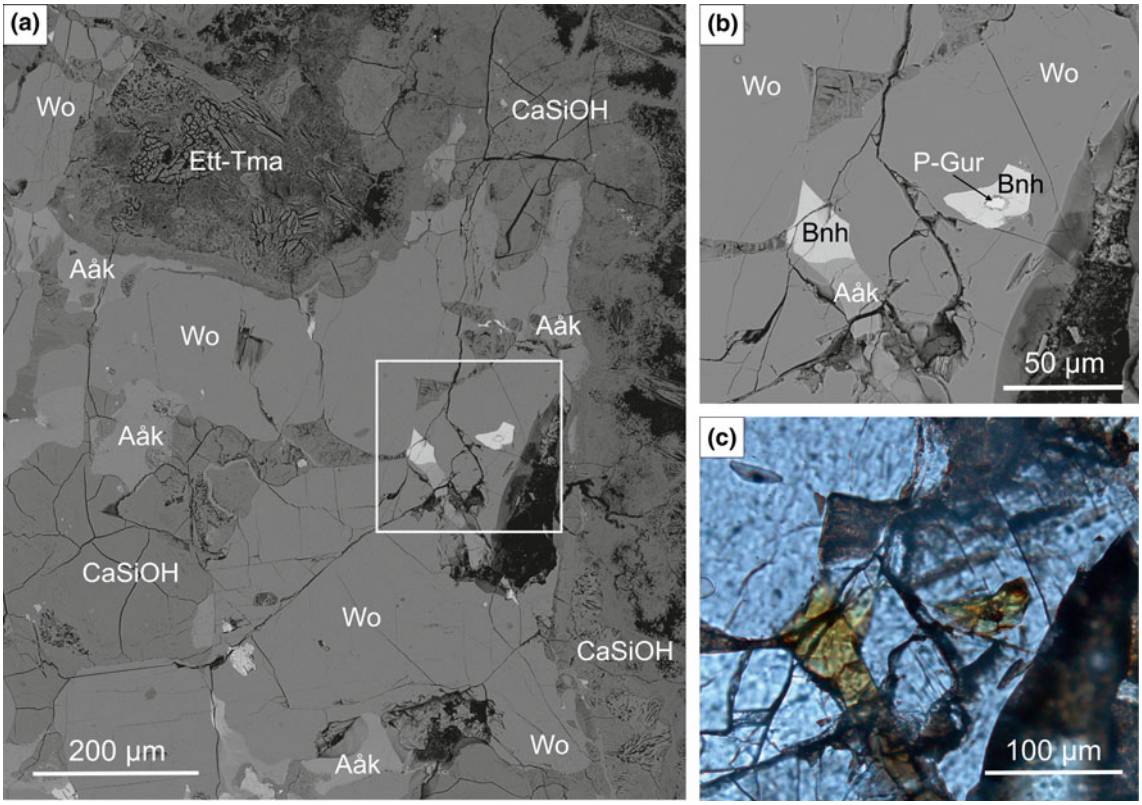

Fig. 1. (a) Mineral association of the carbonate–silicate xenolith; the framed section is magnified in (b), back-scattered electron (BSE) image. (b) Bennesherite and associated minerals, BSE image. (c) Bennesherite crystals with characteristic bright yellow colour, optical image. Aåk –alumoåkermanite; Bnh – bennesherite; CaSiOH – hydrated Ca-aluminosilicates; Ett-Tma – minerals of ettringite–thaumasite series; P-Gur – P-analogue of gurimite; Wo – wollastonite.

for each specimen presented in Table 1, the T2 site is almost fully occupied by Si. Next in allocation, the T1 site is mixed, with a predominance of ferrous iron. Bennesherite from Germany and the holotype locality have a similar content of ~81% of Fe^{2+} at the T1 site whereas the DRC specimen is slightly more ferrous (0.87 apfu). The amount of additional impurities does not exceed 20% of this site occupancy and is represented mainly by Al, Mg, Ti, Mn and Zn, characteristic for melilite group minerals.

Bennesherite crystals presented in Fig. 1 were extracted for single-crystal X-ray diffraction analysis. However, we failed to collect diffraction data due to intergrowths and poor quality of crystals. Nevertheless, identification of bennesherite was confirmed by the detailed Raman spectroscopy investigation described below.

According to the factor-group analysis of the melilite-type structure, 28 (only for the Si_2O_7 group) or 45 Raman active modes were predicted by Hanuza *et al.* (2012) and Sharma *et al.* (1988), respectively. In the Raman spectrum of bennesherite from the Bellerberg volcano, presented in Fig. 2a, 34 bands are observed. In comparison with the published data, their higher or lower number can be related to the deconvolution and curve fitting (Gaussian–Lorentzian functions) of the component bands or low intensity and random degeneration. As the relevant band ascription is often found in Raman spectroscopy literature for natural and synthetic melilites, some authors have used the data of calculated and measured spectra of other phases containing Si_2O_7 groups and tried to determine the ranges of band vibrations (Sharma *et al.*, 1983, 1988; Dowty, 1987; Bouhifd *et al.*, 2002; Marincea *et al.*, 2011; Hanuza *et al.*, 2012; Allu *et al.*, 2017; Ogorodova *et al.*, 2018; Krzątała *et al.*, 2022).

On the basis of available knowledge, consecutive Raman band assignment for bennesherite is proposed in this present work. In the spectral region 850–1050 cm^{-1} symmetric and asymmetric vibrations related to the disilicate $(Si_2O_7)^{6-}$ group appear. More precisely, the intense bands at 973 cm^{-1} and doublet placed at 903 and 925 cm^{-1} with two weak shoulders at 889 and 948 cm^{-1}, respectively, are assigned to the symmetric stretching vibrations of lateral SiO_3 (terminal nonbridging oxygens of SiO_4 tetrahedra). A broad band with two components at 1026 and 1041 cm^{-1} is attributed to the asymmetric stretching (Si–O–Si) vibrations (bridging oxygen between two Si-tetrahedra in Si_2O_7).

The most intense bands centred at 589 and 618 cm^{-1} with three shoulders at 634, 649 and 673 cm^{-1} correspond to the vibrations of T1 – $Fe^{2+}O_4$ and T2 – Si_2O_7. The Raman band at 589 cm^{-1} is related to the symmetric stretching vibrations of the $(Fe^{2+}O_4)^{6-}$ group, in which the Fe atom is located at the 2a site of the $\bar{4}$ point group symmetry. The other bands belong to the symmetric stretching (Si–O–Si) modes of the Si_2O_7 unit. Due to the high intensity, bands observed in the range 585–620 cm^{-1} may overlap with those attributed to the symmetric bending vibrations of SiO_3 (Hanuza *et al.*, 2012). Next to this spectral region, a single band at 718 cm^{-1} is detected (Fig. 2a). The assignment of this band is problematic because it has not been observed in spectra of other melilite minerals. Krzątała *et al.* (2022), in the spectrum of bennesherite from Israel, found a band at 702 cm^{-1} and ascribed it as a band with mixed nature related to the ν_s(Si–O–Si) and $\nu_s(SiO_3)$ vibrations. In our opinion, the same assignment for the band at 718 cm^{-1} is questionable. According to the calculated wavenumbers for hardystonite, an intense peak at 839 cm^{-1} and two bands at 799 and 819 cm^{-1} in the

https://doi.org/10.1180/mgm.2022.62 Published online by Cambridge University Press

Table 1. The representative chemical composition (wt.%) of bennesherite from three different localities.

	Caspar quarry, Bellerberg volcano, Germany[1]			Gurim Anticline, Hatrurim Complex, Israel[2]			Nyiragongo volcano, DRC[3]		
Constituent	Mean $n = 11$	S.D.	Range	Mean $n = 11$	S.D.	Range	Mean $n = 7$	S.D.	Range
SiO_2	26.76	0.92	25.46–28.03	25.10	0.42	24.35–25.75	24.05	0.59	23.44–25.19
TiO_2	1.10	0.32	0.55–1.72	n.d.			1.36	0.95	0.87–3.49
Al_2O_3	0.52	0.13	0.38–0.81	0.55	0.08	0.44–0.67	0.43	0.17	0.34–0.81
Fe_2O_3	-			0.07*			-		
MgO	0.46	0.24	0.18–0.85	0.74	0.20	0.45–1.10	0.14	0.05	0.07–0.23
CaO	5.46	1.61	3.54–7.79	2.95	0.64	2.41–4.40	1.57	0.54	0.67–2.40
MnO	0.41	0.14	0.00–0.55	0.28	0.08	0.16–0.41	0.27	0.06	0.16–0.32
FeO	12.83	0.66	11.55–13.51	12.21	0.95	10.88–13.81	13.04	1.47	10.02–14.83
ZnO	0.13	0.10	0.00–0.34	0.26	0.06	0.18–0.35	n.d.		
SrO	5.31	2.04	2.65–8.67	0.93	0.28	0.50–1.65	4.67	0.78	3.60–6.02
BaO	45.76	4.79	39.84–53.08	55.23	1.42	51.35–56.38	52.31	1.95	48.91–55.34
Na_2O	0.35	0.13	0.18–0.55	0.17	0.03	0.13–0.22	0.22	0.04	0.18–0.28
K_2O	0.23	0.06	0.14–0.33	0.16	0.03	0.11–0.21	0.43	0.18	0.29–0.82
Total	99.32			98.65			98.49		
Calculated on the basis of 7 O									
Ca^{2+}	0.43			0.25			0.13		
Sr^{2+}	0.23			0.04			0.22		
Ba^{2+}	1.32			1.71			1.64		
Na^{+}	0.05			0.03			0.03		
K^{+}	0.02			0.02			0.04		
Sum X	2.05			2.05			2.06		
Ti^{4+}	0.06			-			0.08		
Al^{3+}	0.04			0.05			0.04		
Fe^{3+}	-			<0.01			-		
Mg^{2+}	0.05			0.09			0.02		
Mn^{2+}	0.03			0.02			0.02		
Fe^{2+}	0.79			0.81			0.87		
Zn^{2+}	0.01			0.01			-		
Sum T1	0.98			0.98			1.03		
Si^{4+}	1.97			1.98			1.92		
SumT2	1.97			1.98			1.92		

Notes: S.D. = 1σ standard deviation; *n* – number of analyses; n.d. – not detected; *calculated based on charge balance; [1] – present study; [2] – Krzątała *et al.* (2022); [3] – Andersen *et al.* (2014).

bennesherite spectrum may also have a mixed nature and have been ascribed to the asymmetric stretching modes of SiO_3 and out-of-plane γ bending (Si–O–Si) vibrations (Hanuza *et al.*, 2012).

The spectral range at 400–515 cm^{-1} is related to the various types of deformation vibrations (δ) and translational modes (T^{*}) of cations and large structural units (Sharma *et al.*, 1988; Ogorodova *et al.*, 2018). Several Raman bands with variable intensities placed at 407, 420, 434, 448, 470, 490 and 508 cm^{-1} are assigned to the asymmetric bending modes of lateral SiO_3 and in-plane bending vibration of internal (Si–O–Si), which are coupled with the (Ba^{2+}) translations (Fig. 2a). Sharma *et al.* (1988) identified the Raman bands in the spectral region between 230–360 cm^{-1} as torsional vibrations of SiO_3. In the bennesherite spectrum, a few bands are observed in this range (Fig. 2a). In addition, an intense band at 308 cm^{-1} with two shoulders at 319 and 337 cm^{-1} can also be coupled with the lattice vibrational modes of Ba translations. Bands at 228, 243, 263 and an intense peak at 272 cm^{-1} are described as rocking ρ lateral SiO_3 vibrations (Hanuza *et al.*, 2012). The Ba–O and lattice vibrations are recorded under 200 cm^{-1} in the bennesherite spectrum (Fig. 2a).

In Fig. 2b, significant differences are observed in the Raman spectrum of bennesherite, measured on the same crystal in a different orientation. Some components in several spectral ranges have been reduced, but wavenumbers are quite similar to those detected in the spectrum shown in Fig. 2a. Only the band assigned to the symmetric stretching vibrations of (Si–O–Si) in the disilicate group placed at 618 cm^{-1}, with a shoulder at 634 cm^{-1}, is characterised by higher intensity (Fig. 2b). A single band at 589 cm^{-1} in Fig. 2a, related to the $(Fe^{2+}O_4)^{6-}$ symmetric stretching vibrations of T1 tetrahedra, now appears as a low intense band with frequency at 595 cm^{-1} on the slope of the more intense Raman band. Several bands have a broad character in the spectral range 800–1030 cm^{-1} compared to the same bands in Fig. 2a. The same dependence is reported for bands attributed to various bending modes in the range 400–460 cm^{-1} (Fig. 2b). Of the several components, only two broader peaks at 409 and 459 cm^{-1} remain. The number of Raman bands associated with the torsional SiO_3 vibrations in the range 230–360 cm^{-1} (Fig. 2b) is comparable with the spectrum in Fig. 2a. The difference is connected only with the band intensities. This characteristic feature is observed in the lowest spectral region. Three bands absent in the first orientation appear in the Raman spectrum with frequencies at 150, 173 and 184 cm^{-1}. This is appropriate because all these bands are related to the Ba–O vibrations (Fig. 2b).

The description of the bennesherite Raman spectrum presented above is in good agreement with the spectral band-range assignments given in many works on the spectroscopic investigation of the melilite-group minerals (Sharma *et al.*, 1983, 1988; Dowty, 1987; Bouhifd *et al.*, 2002; Hanuza *et al.*, 2012; Allu *et al.*, 2017; Ogorodova *et al.*, 2018). Moreover, our data are very similar to the results obtained by Krzątała *et al.* (2022), which performed the first Raman analyses for bennesherite found in rankinite paralava from the Hatrurim Complex in Israel. Nevertheless, on the basis of the spectroscopic data for

https://doi.org/10.1180/mgm.2022.62 Published online by Cambridge University Press

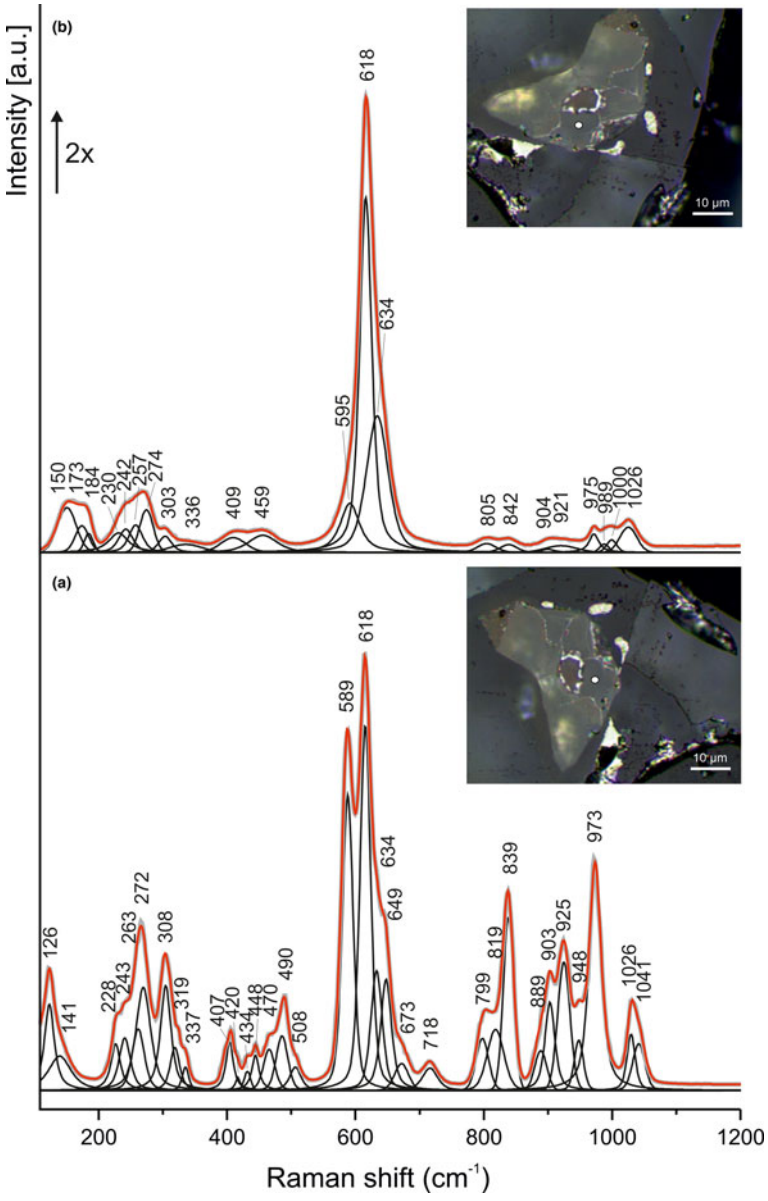

Fig. 2. Raman spectra of bennesherite obtained in a random section at the two orientations relative to a polarised laser beam. The analysis points are shown as a white spot in the optical images inset.

synthetic and natural minerals of the melilite group, the spectral range for symmetric vibrational modes (T–O–T) is located between ~620–670 cm^{-1} (Sharma *et al.*, 1983, 1988; Dowty, 1987; Allu *et al.*, 2017). For åkermanite, hardystonite and Na-melilite, the frequencies of the most intense bands from this region lay between 650–660 cm^{-1} (Sharma *et al.*, 1988; Allu *et al.*, 2017; Ogorodova *et al.*, 2018). For gehlenite, the Raman band related to the ν_s(T–O–T) modes is centred at 626 cm^{-1} (Sharma *et al.*, 1988). For different melilite-group members, it was proved that the frequencies of ν_s(T–O–T) bands show a linear dependence with bridging T–O–T angle, i.e. the greater the T–O–T angle of the Si_2O_7 unit, the higher the frequencies of Raman bands attributed to the symmetric stretching (T–O–T) modes of the disilicate group (Sharma *et al.*, 1988). However for bennesherite, this dependence is troubling. The structural data obtained for Israeli bennesherite indicated that the value of the T–O–T angle equals 142.9° (Krzątała *et al.*, 2022). Considering the data published by Sharma *et al.* (1988), the wavenumber of the most intense band, with such an angle, should be observed at ~670 cm^{-1} in the Raman spectrum. For comparison, in åkermanite, the T–O–T angle is ~139.4° and the Raman band is detected at 664 cm^{-1} (Sharma *et al.*, 1988). Spectroscopic data in the present work for Bellerberg bennesherite show that the prominent peak assigned to ν_s(T–O–T) lies at 618 cm^{-1}. In addition, in the Raman spectrum for bennesherite from the Hatrurim Complex, the wider band centred at 635 cm^{-1}, with a shoulder at 611 cm^{-1} (Krzątała *et al.*, 2022), also corresponds to our results. The frequencies in both specimens are shifted to the lower values despite having the largest T–O–T angle values reported for melilites. In this case, the heavy eight-fold coordinated Ba atom, which occupies the X position in the crystal structure, played a significant role in decreasing the band frequencies. In previous work, only melilites with Ca at the X site were included, hence the Raman bands used by Sharma *et al.* (1988) for the correlation with T–O–T angle were in a higher spectral region.

https://doi.org/10.1180/mgm.2022.62 Published online by Cambridge University Press

Other melilite-group minerals

Semi-quantitative data from SEM–EDS analyses along with quantitative data from electron microprobe analyses also revealed the presence of other melilite-group minerals in carbonate–silicate xenoliths from the Bellerberg volcano. Selected chemical composition results for these mineral phases are correlated in Table 2. Gehlenite, identified as a rock-forming mineral in an altered part of the xenolith, exhibits a fairly standard composition for Al, which almost fully occupies the T1 and partially the T2 sites. Compared to other melilites in Table 2, gehlenite contains a nonsignificant amount of Fe. Alumoåkermanite and potentially new minerals 'Fe^{2+}-åkermanite' and 'Sr-bennesherite' occur, similarly to bennesherite, in non-altered fragments of xenolith, usually in interstitial areas between the wollastonite and nepheline crystals. However, alumoåkermanite forms bigger crystals, up to as much as 200 μm in size, as shown in Fig. 1, whereas the crystals of the other two melilites do not exceed 40 μm. Alumoåkermanite is enriched in Sr^{2+} at the X site and has mixed occupancy at the T1 site with dominant Al and additional Mg and Fe^{2+}. The average SrO content is variable, and for individual analyses ranges from 1.03 to 5.97 wt.%. This enrichment is significant in almost all melilite-group minerals observed in non-altered fragments of xenolith (Tables 1, 2), which, conversely, was not detected for the exact counterparts in paralavas of the Hatrurim Complex despite the similar mineral association (Krzątała *et al.* 2020).

'Fe^{2+}-åkermanite', 'Sr-bennesherite' (Table 2) and bennesherite (Table 1), are the most ferrous melilites in the samples analysed. The quantity of Fe increases with simultaneous decrease in Al content in the following sequence for melilite-type minerals: alumoåkermanite → 'Fe^{2+}-åkermanite' → bennesherite → 'Sr-bennesherite' (Table 1, 2). Other investigations have noted a similar observation for some ferrous melilites (Andersen *et al.* 2014; Krzątała *et al.* 2022). This condition may be related to the crystal chemistry, which determines the stabilisation of ferrous iron into the structure of some melilites (Krzątała *et al.* 2022), or suggests that here is a deficient ferric iron activity in tetrahedral coordination in highly alkaline melts (Andersen *et al.* 2014). The distribution of the three dominant cations, Ca, Ba and Sr, at the X site is variable, which manifests in the different apfu content for ferrous melilite end-members in the ternary $Ba_2Fe^{2+}Si_2O_7$–$Ca_2Fe^{2+}Si_2O_7$–$Sr_2Fe^{2+}Si_2O_7$ phase system (Fig. 3). At the T1 site, Fe^{2+} dominates over the following elements (Ti, Al, Mg, Mn and Zn), which means that more than half of this site is occupied by ferrous ions (Tables 1, 2). Nevertheless, the obtained chemical data for ferrous melilites recognised in xenolith samples shows that 'Sr-bennesherite' and 'Fe^{2+}-åkermanite' can be distinguished as new members from other melilite-group minerals (Fig. 3).

Rare accessory Ba minerals

Walstromite

Walstromite, $BaCa_2Si_3O_9$, a three-membered $(Si_3O_9)^{6-}$ cyclosilicate, was described for the first time from sanbornite-bearing metamorphic rocks in Rush Creek and Big Creek, Eastern

Table 2. Selected chemical compositions of melilites from analysed xenolith samples.

	Gehlenite			Alumoåkermanite				Fe^{2+}-åkermanite				Sr-bennesherite		
Constituent	Mean *n* = 10	S.D.	Range	Mean *n* = 3	Mean *n* = 14	S.D.	Range	Mean *n* = 3	Mean *n* = 8	S.D.	Range	Mean *n* = 7	S.D.	Range
SiO_2	32.20	0.78	31.08–33.20	42.36	41.84	0.70	40.99–43.04	38.74	36.50	1.29	34.10–37.94	30.86	1.16	29.85–32.68
TiO_2	n.d.			n.d.	n.d.			n.d.	0.08	0.07	0.00–0.20	0.12	0.10	0.00–0.25
Al_2O_3	26.15	0.81	24.84–27.25	7.29	7.56	1.07	5.93–9.81	5.65	3.44	0.24	3.09–3.76	0.80	0.51	0.38–1.55
Fe_2O_3	1.70	0.43	0.94–2.37	-	-			-	-			-		
MgO	0.25	0.23	0.05–0.66	5.11	4.07	0.78	2.98–5.61	1.65	2.29	0.72	0.74–2.97	0.04	0.06	0.00–0.18
CaO	33.72	2.02	29.90–37.19	25.17	30.01	2.69	24.37–32.96	26.25	18.72	1.76	15.87–20.75	9.81	1.94	7.7712.38
MnO	n.d.			0.07	0.23	0.06	0.14–0.32	0.41	0.36	0.07	0.28–0.46	0.45	0.38	0.06–1.07
FeO	-			5.40	7.17	1.03	5.28–8.40	12.05	11.91	0.79	11.23–13.70	15.93	0.31	15.62–16.41
ZnO	n.d.			0.25	0.24	0.09	0.14–0.40	0.37	0.43	0.07	0.34–0.50	0.57	0.10	0.37–0.66
SrO	1.11	0.87	0.35–3.41	5.32	2.82	1.76	1.03–5.97	4.65	12.29	1.55	10.42–14.63	23.23	1.11	21.79–24.34
BaO	n.d.			1.46	1.13	0.71	0.40–2.57	6.21	9.03	1.53	6.71–11.37	12.84	5.12	5.93–18.26
Na_2O	4.09	0.81	2.60–5.37	6.37	4.40	0.72	3.38–5.89	3.18	2.86	0.87	1.89–3.91	0.86	0.34	0.59–1.32
K_2O	n.d.			0.19	0.25	0.05	0.19–0.39	0.36	0.31	0.06	0.24–0.45	0.24	0.04	0.20–0.31
Total	99.22			98.99	99.72			99.52	98.22			95.76		
Calculated on the basis of 7 O														
Ca^{2+}	1.65			1.28	1.52			1.44	1.11			0.68		
Sr^{2+}	0.03			0.15	0.08			0.14	0.39			0.88		
Ba^{2+}	-			0.03	0.02			0.12	0.20			0.33		
Na^{+}	0.36			0.59	0.40			0.32	0.31			0.11		
K^{+}	-			0.01	0.02			0.02	0.02			0.02		
Sum X	2.04			2.06	2.04			2.04	2.03			2.02		
Ti^{4+}	-			-	-			-	<0.01			0.01		
Al^{3+}	0.92			0.41	0.42			0.34	0.22			0.06		
Fe^{3+}	0.06			-	-			-	-			-		
Mg^{2+}	0.02			0.36	0.29			0.13	0.19			<0.01		
Mn^{2+}	-			<0.01	0.01			0.02	0.02			0.02		
Fe^{2+}	-			0.22	0.28			0.51	0.55			0.87		
Zn^{2+}	-			0.01	0.01			0.01	0.02			0.03		
Sum T1	1.00			1.00	1.01			1.01	1.00			1.00		
Si^{4+}	1.47			2.02	1.98			1.98	2.01			2.01		
Al^{3+}	0.48			-	-			-	-			-		
Sum T2	1.95			2.02	1.98			1.98	2.01			2.01		

Notes: S.D. = 1σ standard deviation; *n* – number of analyses; n.d. – not detected.

https://doi.org/10.1180/mgm.2022.62 Published online by Cambridge University Press

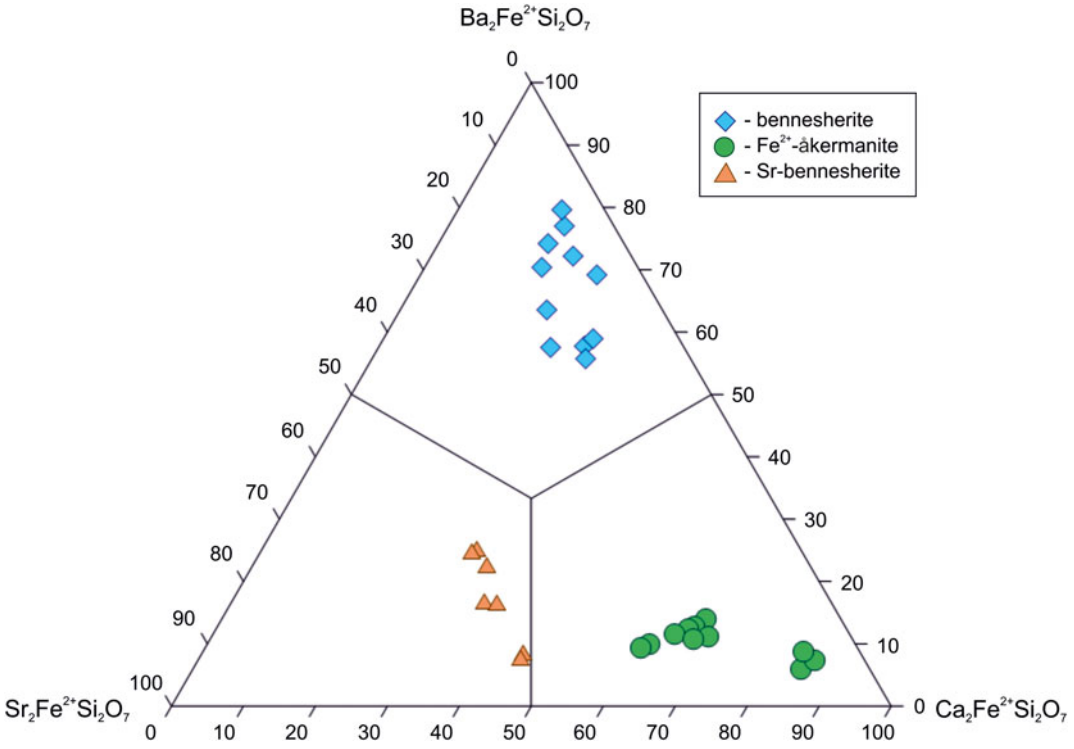

Fig. 3. Ternary phase diagram for ferrous melilite members detected in xenolith samples from Bellerberg volcano, Germany.

Fresno County, California, USA (Alfors *et al.*, 1965). Subsequently, it has also been recognised in several deposits along the Western Margin of North America (from Baja California Norte in Mexico to Western Canada and Alaska) (Dunning and Cooper, 1999; Dunning, 2018; Dunning and Walstrom, 2018). Later, walstromite was reported in paralavas from the pyrometamorphic Hatrurim Complex in Israel (Krzątała *et al.*, 2020) and from the Jakobsberg Mn–Fe deposit, Värmland, Sweden (Holtstam *et al.*, 2021). Together with margarosanite, $PbCa_2Si_3O_9$ and breyite, $Ca_3Si_3O_9$, walstromite forms the margarosanite group (Holtstam *et al.*, 2021).

Walstromite, identified for the first time in carbonate–silicate xenoliths from the Bellerberg volcano, forms colourless subhedral and anhedral crystals (Fig. 4), variable in size, though frequently 30–100 μm. Typically, walstromite crystals fill the space between nepheline and wollastonite grains (Fig. 4a) or in cracks in large wollastonite crystals (Fig. 4b,c). Another Ba-bearing mineral, fresnoite, occurs in association with walstromite (Fig. 4c).

Electron-microprobe analyses of walstromite from Caspar quarry, two outcrops of the Hatrurim Complex in Israel (Gurim Anticline and Zuk Tamrur) and Fresno County in the USA (holotype locality) are correlated in Table 3. The calculated empirical formula for the German specimen is as follows $(Ba_{0.90}Sr_{0.11})_{\Sigma 1.01}(Ca_{1.97}Fe_{0.01})_{\Sigma 1.98}(Si_{2.99}Ti_{0.01}Al_{0.01})_{\Sigma 3.01}O_9$. By comparison of these data for walstromite from different localities, we can conclude that this mineral has a stable composition (Table 3).

The holotype walstromite composition was measured originally using a direct current arc emission spectrograph and the totals of analyses were normalised to 100% from instrumental totals (Alfors *et al.*, 1965). In this paper, these two analyses were recalculated without this normalisation. The obtained results are very similar to the original one. The slight differences in apfu values of each element were <0.05 (Table 3). The only significant feature noted between the chemical results for walstromite samples presented in Table 3 is the amount of SrO. For German walstromite, this content is equal to ~2.50, for some individual analyses even ~3.00 wt.%, which corresponds to 0.10 apfu in the chemical formula, whereas the Sr content from previous investigations was <0.02 apfu (Alfors *et al.*, 1965; Krzątała *et al.*, 2020). The increased Sr content in German samples corresponds to a decrease in Ba, indicating mutual substitution within the one structural site.

Energy dispersive spectroscopy analysis of walstromite samples from the Jakobsberg Mn–Fe deposit in Sweden found Pb substitution for Ba (Holtstam *et al.*, 2021). Such substitution has not been reported in other mentioned localities (Table 3). This occurrence is related to the mineral association because, in the Jakobsberg deposit, walstromite occurs together with margarosanite. As noted by Holtstam *et al.* (2021), both minerals contain variable Ba–Pb amounts, indicating a solid-solution series between them

In the Raman spectrum of walstromite from the carbonate–silicate xenolith a sharp and intense band at ~650 cm^{-1} is observed (Fig. 5). This Raman band is typical for ring silicates (cyclosilicates) and is related to the Si–O–Si symmetric vibrations of the three-membered $(Si_3O_9)^{6-}$ rings. The next intense band that occurs at 987 cm^{-1} is assigned to the symmetric Si–O vibrations of the $(SiO_4)^{4-}$ group with a non-bridging environment. In other words, this band corresponds to the vibrations between the Si atom and apical oxygen atoms in each tetrahedron. Moreover, three bands with lower intensities at 904, 918 and 940 cm^{-1} are observed in the walstromite spectrum. Previous publications have no information about these Raman bands (Gaft *et al.*, 2013; Krzątała *et al.*, 2020). According to the infrared investigations of some $(Si_3O_9)^{-}$ ring silicates (Sitarz *et al.*, 1997), the assignment of bands in this spectral region might be similar to

https://doi.org/10.1180/mgm.2022.62 Published online by Cambridge University Press

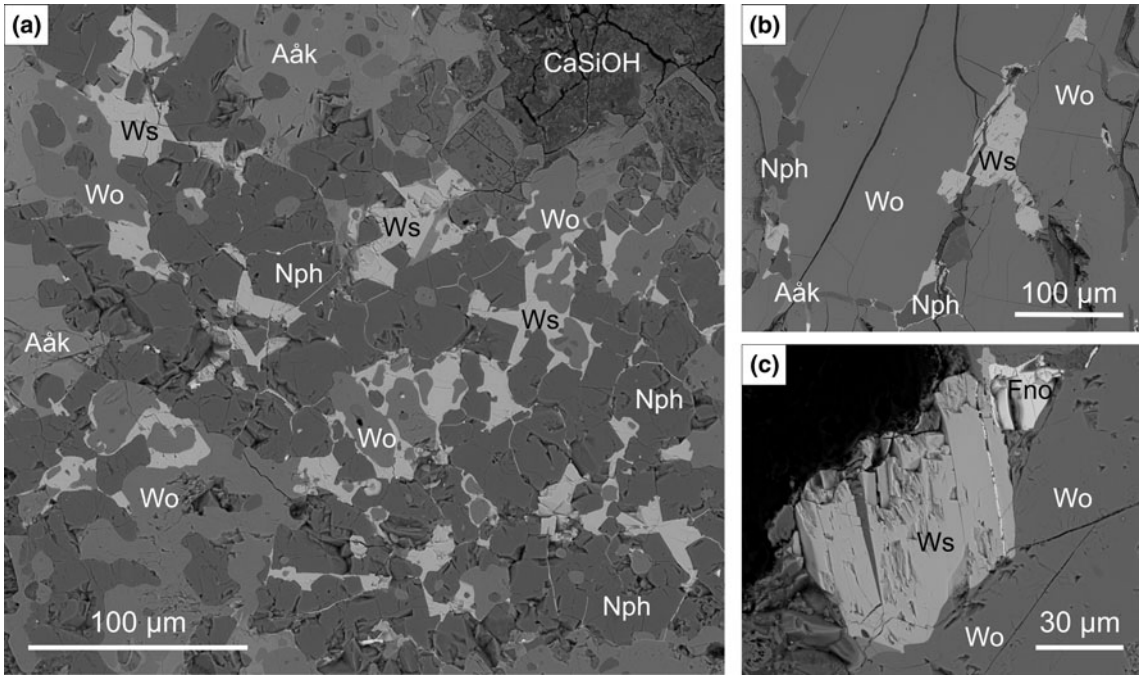

Fig. 4. (a–c) Walstromite and associated minerals in the xenolith samples from the Bellerberg volcano, BSE images. Aåk – alumoåkermanite; CaSiOH – hydrated Ca-aluminosilicates; Fno – fresnoite; Nph – nepheline; Wo – wollastonite; Ws – walstromite.

the Raman band at 987 cm^{-1}. Above 1000 cm^{-1}, two bands with distinct intensity were detected and assigned to asymmetric Si–O stretching vibrations in the $(Si_3O_9)^{6-}$ rings. The spectral region between 400 cm^{-1} and 550 cm^{-1} is related to the three-membered rings Si–O–Si and O–Si–O bending vibrations. Several Raman bands below 400 cm^{-1}, magnified in Fig. 5, correspond to the stretching Ca–O and Ba–O vibrations.

In the current work, the assignment of a low intense Raman band at 581 cm^{-1} is not considered. This band needs detailed investigation because it could be related to the bending vibrations,

Table 3. The representative chemical composition (wt.%) of walstromite from different localities.

	Caspar quarry, Bellerberg Volcano, Germany[1]			Gurim Anticline, Hatrurim Complex, Israel[2]			Zuk Tamrur, Hatrurim Complex, Israel[2]			Eastern Fresno County, USA[3]	
Constituent	Mean $n = 8$	S.D.	Range	Mean $n = 15$	S.D.	Range	Mean $n = 5$	S.D.	Range	$n = 1$	$n = 1$
SiO_2	40.83	0.19	40.57–41.18	40.56	0.40	39.92–41.10	40.19	0.75	39.07–41.10	39.60	38.80
TiO_2	0.25	0.04	0.18–0.29	0.16	0.10	0–0.34	0.34	0.07	0.24–0.43	<0.01	0.03
Al_2O_3	0.15	0.03	0.11–0.20	0.15	0.02	0.12–0.19	0.16	0.04	0.12–0.21	0.07	n.d.
MgO	<0.01			n.d.			n.d.			<0.05	<0.10
CaO	25.17	0.26	24.82–25.49	25.60	0.47	24.84–26.15	24.89	0.39	24.43–25.41	26.10	26.20
MnO	<0.01			n.d.			n.d.			0.33	0.18
FeO	0.13	0.05	0.04–0.18	n.d.			n.d.			<0.02	<0.01
SrO	2.49	0.26	2.19–2.95	0.27	0.20	0–0.68	0.18	0.11	0.09–0.35	0.53	n.d.
BaO	31.34	0.25	31.02–31.75	33.62	0.41	32.90–34.26	32.62	0.60	32.18–33.43	33.30	34.50
Na_2O	<0.09			0.06	0.02	0–0.09	0.15	0.01	0.07–0.11	n.d.	n.d.
K_2O	<0.09			<0.03			n.d.			<0.05	<0.05
Total	100.35			100.42			98.53			99.93	99.71
Calculated on the basis of 9 O											
Ca^{2+}	1.97			2.02			1.99			2.08	2.12
Mn^{2+}	-			-			-			0.02	0.01
Fe^{2+}	0.01			-			-			-	-
Sr^{2+}	0.11			0.01			0.01			0.02	-
Ba^{2+}	0.90			0.97			0.95			0.97	1.02
Na^{+}	-			0.01			0.02			-	-
Sum A + B	2.99			3.01			2.97			3.09	3.15
Si^{4+}	2.99			2.98			3.00			2.95	2.92
Ti^{4+}	0.01			0.01			0.02			-	-
Al^{3+}	0.01			0.01			0.01			0.01	-
Sum T	3.01			3.00			3.03			2.96	2.92

Footnotes: S.D. = 1σ standard deviation; n – number of analyses; n.d. – not detected; [1] – present study; [2] – Krzątała *et al.* (2020); [3] – Alfors *et al.* (1965).

https://doi.org/10.1180/mgm.2022.62 Published online by Cambridge University Press

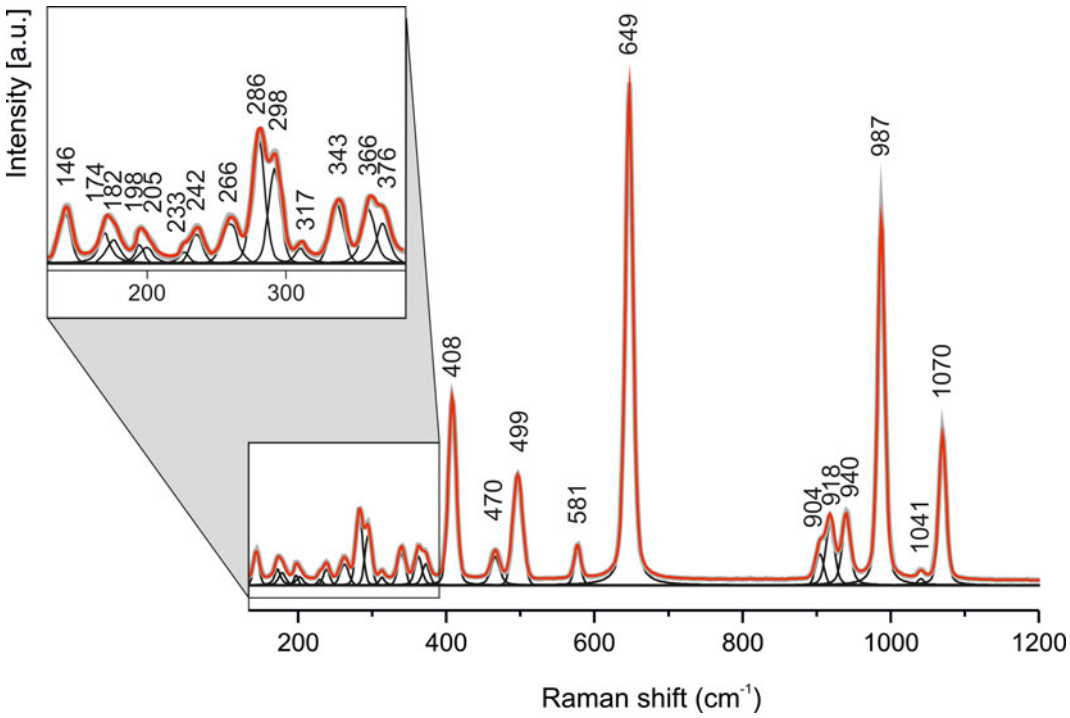

Fig. 5. Raman spectrum of walstromite from Caspar quarry, Bellerberg volcano, Germany.

as proposed by Krzątała *et al.* (2020), or stretching vibrations of the $(Si_3O_9)^{6-}$ rings by analogy to the pseudowollastonite spectrum, which is one of the dominant bands (Richet *et al.*, 1998).

The Raman spectrum of walstromite from Caspar quarry and Raman spectra obtained for specimens from Gurim Anticline in Israel (Krzątała *et al.*, 2020) and Fresno County in California (Gaft *et al.*, 2013) are similar. They exhibit the same band features, e.g. the band frequencies related to the Si–O–Si stretching vibrations of the $(Si_3O_9)^{6-}$ rings, which are observed at 649 cm^{-1} (present study), 651 cm^{-1} (Krzątała *et al.*, 2020) and 650 cm^{-1} (Gaft *et al.*, 2013), respectively. Similar correlations are also detected for other types of vibrations and band positions. Moreover, the resemblance between the Raman spectrum of walstromite and two other minerals of the margarosanite group: breyite and margarosanite, is significant. The main difference was noted in the margarosanite spectrum, which reflects the intense band with unclear nature at 1013 cm^{-1}, not presented in the Raman spectra of the other two minerals (Krzątała *et al.*, 2020).

Fresnoite

Similarly to walstromite, fresnoite, $Ba_2TiO(Si_2O_7)$ was discovered in sanbornite metamorphic deposits from Eastern Fresno County, California, USA (Alfors *et al.*, 1965). In contrast to walstromite, this mineral is more common worldwide and has been recognised in different types of rocks in several localities (Solovova *et al.*, 2009; Andersen *et al.*, 2014; Peretyazhko *et al.*, 2018; Krzątała *et al.*, 2022). Fresnoite has been mentioned previously in Germany in association with schüllerite from the Löhley basalt quarry at the Eifel Volcanic district (Chukanov *et al.*, 2011). Nevertheless, detailed results focusing on this mineral have not been published.

In analysed samples, fresnoite, similar to bennesherite, exhibits a yellow colour in transmitted light. Typically, this mineral forms subhedral and anhedral crystals reaching a size of ~40–50 μm (Fig. 6). They occur in small intergranular areas between rock-forming minerals, mostly wollastonite, nepheline and minerals of the melilite group (Fig. 6a,b). Occasionally, fresnoite–bennesherite intergrowths are observed in xenolith samples (Fig. 6c). The same feature was noted for paralava samples from Israel, where these two phases were associated (Krzątała *et al.*, 2022).

The results of fresnoite chemical analyses from Caspar quarry, together with the data from the type locality – Fresno County and Gurim Anticline, are compared in Table 4. On the basis of eight oxygens, the empirical formula of German fresnoite was calculated as $(Ba_{1.88}Ca_{0.08}Sr_{0.07})_{\Sigma 2.03}(Ti_{0.97}Fe^{2+}_{0.03})_{\Sigma 1.00}(Si_{1.98}Al_{0.03})_{\Sigma 2.01}O_8$. Generally, the data correlated in Table 4 indicate that fresnoite has a consistent composition with insignificant distinctions. Similarly to walstromite, differences between analyses is related mainly to the Sr content. Fresnoite from Bellerberg volcano, in contrast to the samples from other localities, is enriched with this component, which varies from 1.05 to 2.12 wt.% (Table 4). For one sample from Fresno, the amount of SrO was equal to 0.28 wt.%, equivalent to 0.01 apfu. In other samples, Sr was not detected. One of the recalculated original analyses from Fresno County exhibits a higher TiO_2 content with simultaneous lower SiO_2 than other samples presented in Table 4. This may be evidence that Ti occupies not only the T1 but also the T2 site in the crystal structure of fresnoite. However, this assumption was not confirmed by the structural investigation in the previous report from Krzątała *et al.* (2022).

The Raman spectrum of fresnoite from Caspar quarry is presented in Fig. 7. This spectrum is characterised by a sharp and intense Raman band at 859 cm^{-1} with the lower intensity band on the shoulder at a higher frequency ~875 cm^{-1}. These two bands have a complex nature and were assigned to the symmetric stretching SiO_3 vibrations of the disilicate group $(Si_2O_7)^{6-}$ and symmetric stretching (Ti–O) vibrations in the square pyramid $(TiO_5)^{6-}$. In this case, the (Ti–O) vibrations correspond to the short bond between the Ti and oxygen atom located at the apex

https://doi.org/10.1180/mgm.2022.62 Published online by Cambridge University Press

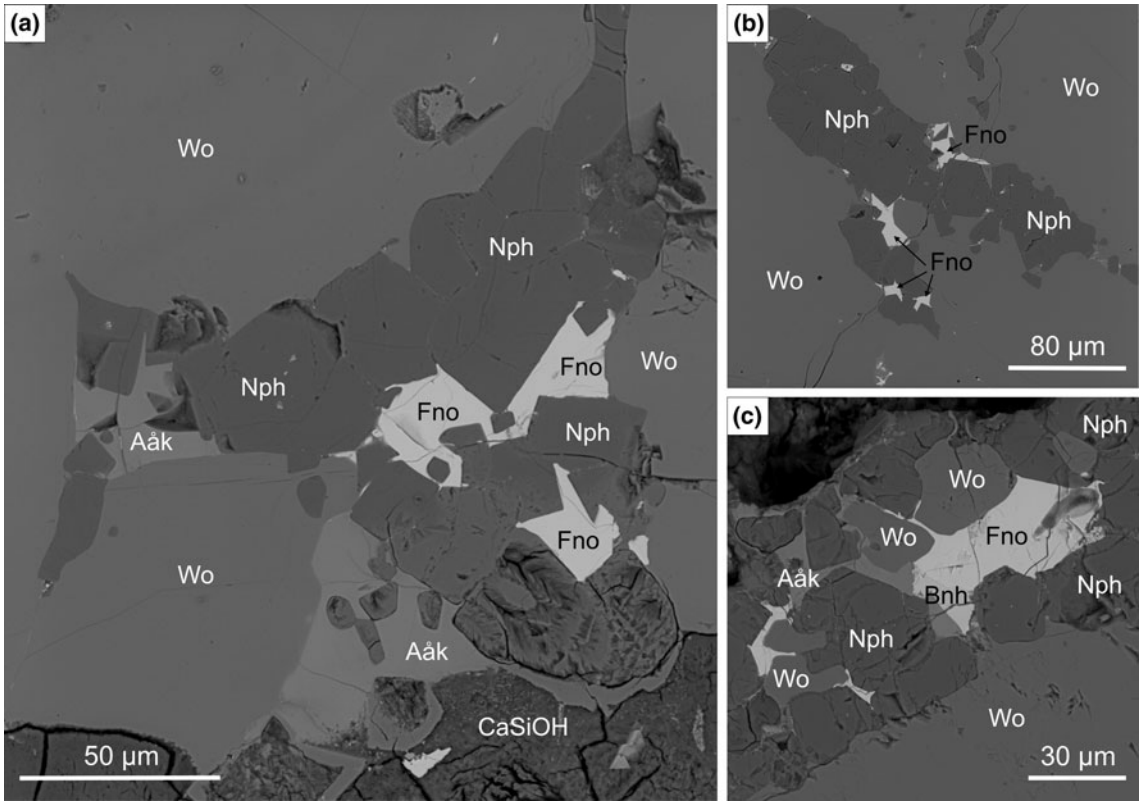

Fig. 6. (a–b) Fresnoite and associated minerals in the xenolith samples from the Bellerberg volcano. (c) Intergrowths of fresnoite and bennesherite. BSE images. Aåk – alumoåkermanite; CaSiOH – hydrated Ca-aluminosilicates; Bnh – bennesherite; Fno – fresnoite; Nph – nepheline; Wo – wollastonite.

Table 4. The representative chemical composition (wt.%) of fresnoite from different localities.

	Caspar quarry, Bellerberg Volcano, Germany[1]			Gurim Anticline, Hatrurim Complex, Israel[2]			Eastern Fresno County, USA[3]	
Constituent	Mean $n = 9$	S.D.	Range	Mean $n = 10$	S.D.	Range	$n = 1$	$n = 1$
SiO_2	23.87	0.16	23.59–24.12	23.82	0.15	23.56–24.09	21.80	23.80
TiO_2	15.51	0.53	14.91–16.35	15.55	0.55	14.50–16.18	17.20	15.20
Al_2O_3	0.35	0.15	0.27–0.76	0.38	0.03	0.32–0.41	0.12	n.d.
Fe_2O_3	-			0.90	0.46	0.28–1.77	-	-
MgO	<0.01			n.d.			<0.05	0.19
CaO	0.94	0.43	0.25–1.59	0.45	0.12	0.19–0.62	0.14	0.55
MnO	<0.01			n.d.			0.027	0.074
FeO	0.42	0.24	0.15–0.90	-			1.00	0.77
SrO	1.41	0.43	1.05–2.12	n.d.			0.28	n.d.
BaO	57.96	0.90	56.47–59.81	58.64	0.24	58.30–59.01	59.40	59.40
Na_2O	n.d.			0.11	0.02	0.08–0.13	n.d.	n.d.
Total	100.46			99.85			99.97	99.98
Calculated on the basis of 8 O								
Ca^{2+}	0.08			0.04			0.01	0.05
Sr^{2+}	0.07			-			0.01	-
Ba^{2+}	1.88			1.91			1.98	1.95
Na^{+}	-			0.02			-	-
Sum X	2.03			1.97			2.00	2.00
Ti^{4+}	0.97			0.97			1.10	0.96
Fe^{3+}	-			0.06			-	-
Mg^{2+}	-			-			-	0.02
Mn^{2+}	-			-			<0.01	0.01
Fe^{2+}	0.03			-			0.07	0.05
Sum T1	1.00			1.03			1.17	1.04
Si^{4+}	1.98			1.98			1.85	2.00
Al^{3+}	0.03			0.04			0.01	-
Sum T2	2.01			2.02			1.86	2.00

Footnotes: S.D. = 1σ standard deviation; *n* – number of analyses; n.d. – not detected; [1] – present study; [2] – Krzątała *et al.* (2022); [3] – Alfors *et al.* (1965).

https://doi.org/10.1180/mgm.2022.62 Published online by Cambridge University Press

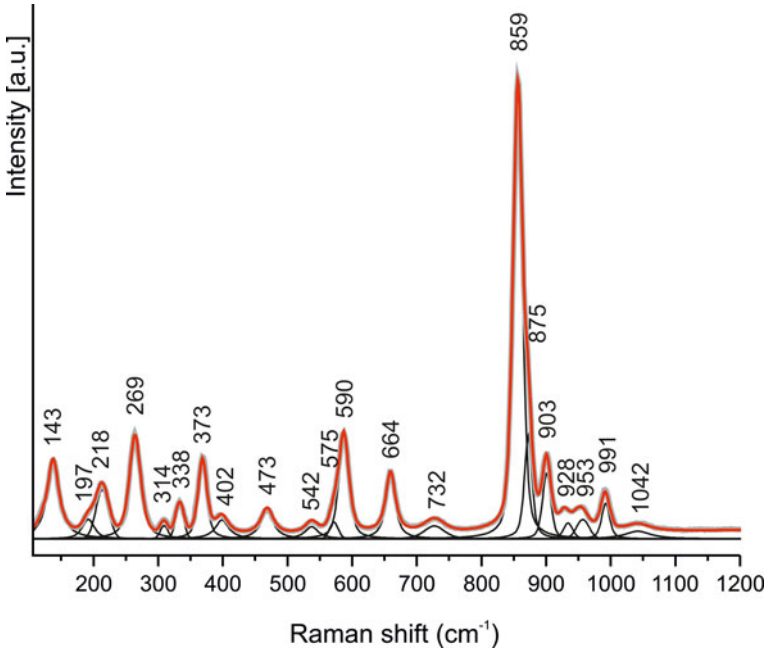

Fig. 7. Raman spectrum of fresnoite from Caspar quarry, Bellerberg volcano, Germany.

of the $(TiO_5)^{6-}$ tetragonal pyramid. The assignment of these bands was confirmed previously for synthetic $Ba_2TiSi_2O_8$, also known as BTS (Gabelica-Robert and Tarte, 1981; Markgraf *et al.*, 1992), and natural fresnoite (Krzątała *et al.*, 2022). The bands in the range ~900–990 cm^{-1} have been assigned to the symmetric and asymmetric (SiO_3) vibrations, whereas the band at 1042 cm^{-1} has been assigned to asymmetric stretching modes of the disilicate group. The latter assignment was confirmed by comparison with the Raman spectrum of the mineral rusinovite, $Ca_{10}(Si_2O_7)_3Cl_2$, which contains a $(Si_2O_7)^{6-}$ group in its structure (Środek *et al.*, 2018). In the Raman spectrum of this mineral, the bands related to the asymmetric stretching vibrations are in the range of 1041–1043 cm^{-1}. The mixing nature of this band, asymmetric bridging Si–O–Si + asymmetric SiO_3 vibrations, cannot be excluded according to the IR spectrum of fresnoite (Gabelica-Robert and Tarte, 1981).

The bridging symmetric stretching Si–O–Si vibrations of the Si_2O_7 group correspond to the Raman band at 664 cm^{-1}. The bands observed between ~540 and 590 cm^{-1} are related to the bending SiO_3 vibrations. Nevertheless, the bands at 590 cm^{-1} may also be connected with TiO_4 vibration from the square $(TiO_5)^{6-}$ pyramid (Dai *et al.*, 2007). The range ~270–400 cm^{-1}, with characteristic bands at 269, 338 and 373 cm^{-1}, has been assigned to the translational and symmetric bending vibration of TiO_5 and Si_2O_7. All bands in the Raman spectrum of fresnoite noted below 250 cm^{-1} are assigned to stretching Ba–O and lattice vibrations. The assignment of two Raman bands at 732 cm^{-1} and 473 cm^{-1} is disputable. According to results obtained for oxide glasses, the first one could be related to the deformation vibrations of O–Ti–O or O–(Si,Ti)–O in sheet units (Yadav and Singh, 2015). In turn, the nature of the second one, which was also detected for fresnoite from the Hatrurim Complex in Israel at 473 cm^{-1}, but not described in detail, is unclear and needs to be investigated further.

The detailed description of the natural fresnoite crystal presented in this work agrees with the spectroscopic result obtained for synthetic counterparts (Gabelica-Robert and Tarte, 1981; Markgraf *et al.*, 1992; Dai *et al.*, 2007; Zhu *et al.*, 2007), and provides additional information not covered by Krzątała *et al.* (2022) which focused on only a few characteristic bands.

Celsian

Celsian, $Ba(Al_2Si_2O_8)$, is a Ba-feldspar belonging to the feldspar group with Al:Si ratio equal to 1:1. It was first described from the Mn–Fe deposits at the Jakobsberg ore field, Värmland, Sweden (holotype, Sjögren, 1895). Since then, celsian has been detected within different types of rocks worldwide (Spencer, 1942; Alfors *et al.*, 1965; Coats *et al.*, 1980; Moro *et al.*, 2001; Dunning, 2018; Krzątała *et al.*, 2020).

In carbonate–silicate xenoliths, celsian is less abundant than walstromite and fresnoite. Usually, it forms anhedral crystals up to 40 μm in size (Fig. 8). Similarly to other Ba-minerals presented in this work, celsian occurs in non-altered xenolith zones between the larger wollastonite, nepheline and alumoåkermanite crystals (Fig. 8a,b).

The electron microprobe analyses of celsian from the Caspar quarry locality are given in Table 5. For comparison, the chemical data of celsian from two additional localities: the baryte deposit of Zamora in Spain (Moro *et al.*, 2001) and Aberfeldy in Scotland (Fortey and Beddoe-Stephens, 1982), are also included in Table 5. The empirical formula of celsian from Germany, calculated on the basis of eight oxygens, is $(Ba_{0.97}Ca_{0.02}Na_{0.02}Sr_{0.01}K_{0.01})_{\Sigma 1.03}(Al_{1.96}Fe_{0.06})_{\Sigma 2.02}Si_{1.98}O_8$. Our result shows that celsian from Caspar quarry is similar to samples from Scotland. The data is similar for the holotype locality, where the main celsian constituents are equal to 32.43 wt.% for SiO_2, 26.55 wt.% for Al_2O_3, and 39.72 wt.% for BaO (Sjögren, 1895). In comparison, celsian samples from Spain exhibit higher BaO content ~41–42 wt.%, lower Al_2O_3 content ~25 wt.%, and a negligible TiO_2.

Perhaps due to the similarity to other spectra of feldspar minerals, there is no description or even qualitative characteristics of the celsian Raman spectrum in the literature. Nevertheless, graphic depictions can be found in the spectroscopic database and in some publications (Galuskina *et al.*, 2017a). In the present work, we proposed the following band assignment based on a previous publication containing Raman spectra characterization of the feldspar-group minerals (Freeman *et al.*, 2008).

https://doi.org/10.1180/mgm.2022.62 Published online by Cambridge University Press

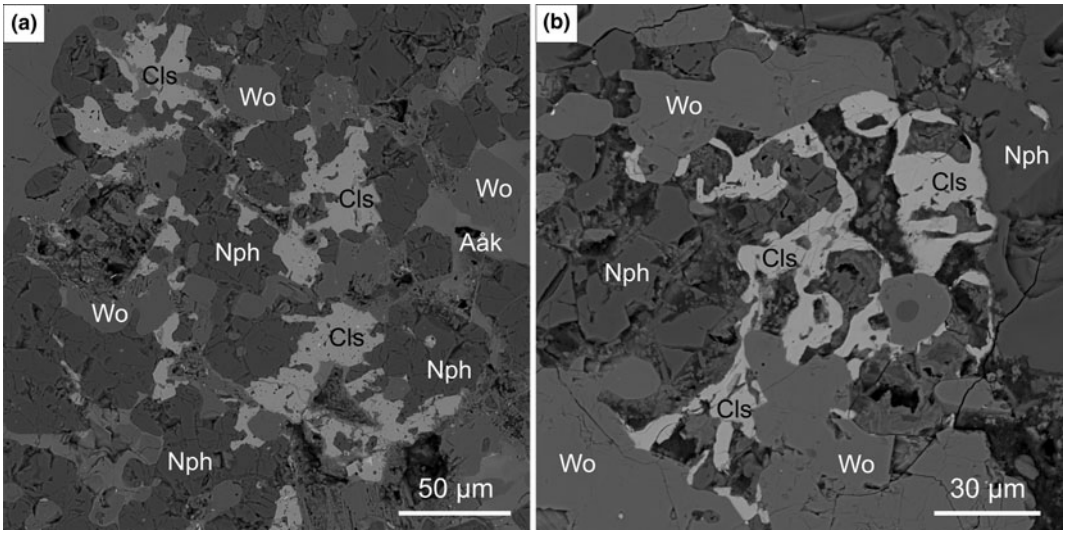

Fig. 8. (a–b) Celsian and associated rock-forming minerals in the xenolith samples, BSE images. Aåk – alumoåkermanite; Nph – nepheline; Wo – wollastonite.

The celsian spectrum from Caspar quarry was divided into a few band groups (Fig. 9). Group I is the spectral range between 450–520 cm^{-1}. Two Raman bands were distinguished, one as a doublet in the range 455–462 and a very strong band at ~509 cm^{-1}, which correspond to the breathing deformation modes of the four-membered rings of the tetrahedron. Group II is the 200–430 cm^{-1} range and contains a few Raman bands of varying intensity at 218, 238 (strong), 250, 306, 356, 391, 410 and 425 cm^{-1}. This group of bands is assigned to the rotation-translation modes of the four-membered ring. Group III below the 200 cm^{-1} is characterised by the strong and intense band at 105 cm^{-1} and a few other bands placed at 130, 169 and 195 cm^{-1}, which are associated with the cage-shear modes. Bands forming group IV are between 590 and 800 cm^{-1} and are ascribed to the deformation modes of the tetrahedra. In the celsian spectrum, consecutive bands were distinguished at 595,

Table 5. Representative compositions (wt.%) of celsian from different localities.

	Caspar quarry, Bellerberg Volcano, Germany[1]			Sedex Deposits, Zamora, Spain[2]				Aberfeldy, Scotland[3]	
Constituent	Mean $n=7$	S.D.	Range	Mean[a] $n=5$	Mean[b] $n=2$	Mean[c] $n=3$	Mean[d] $n=4$	[e] $n=1$	[f] $n=1$
SiO_2	31.81	0.13	31.72–31.90	32.32	32.32	32.06	32.89	31.80	32.64
TiO_2	n.d.			n.d.	0.18	0.01	0.13	n.d.	n.d.
Al_2O_3	26.71	0.20	26.56–26.85	24.90	25.49	24.67	24.75	27.67	27.27
Fe_2O_3	1.20	0.18	1.07–1.33	-	-	-	-	0.28	n.d.
CaO	0.23	0.05	0.20–0.27	0.09	n.d.	0.02	0.01	n.d.	n.d.
MnO	n.d.			n.d.	n.d.	0.01	0.02	n.d.	n.d.
FeO	n.d.			0.03	n.d.	0.16	0.04	-	-
SrO	0.34	0.09	0.27–0.40	n.d.	n.d.	n.d.	n.d.	n.d.	n.d.
BaO	39.58	0.09	39.51–39.65	42.30	40.70	41.39	41.20	39.84	39.43
Na_2O	0.15	0.06	0.10–0.19	0.16	0.25	0.18	0.24	0.08	0.10
K_2O	0.14	0.03	0.12–0.16	0.17	0.29	0.18	0.34	0.31	0.33
Total	100.16			99.97	99.23	98.68	99.62	99.98	99.77
Calculated on the basis of 8 O									
Ca^{2+}	0.02			0.01	-	<0.01	<0.01	-	-
Sr^{2+}	0.01			-	-	-	-	-	-
Ba^{2+}	0.97			1.06	1.01	1.05	1.03	0.97	0.96
Na^{+}	0.02			0.02	0.03	0.02	0.03	0.01	0.01
K^{+}	0.01			0.01	0.02	0.01	0.03	0.02	0.03
Sum A	1.03			1.10	1.06	1.08	1.09	1.00	1.00
Ti^{4+}	-			-	0.01	<0.01	0.01	-	-
Al^{3+}	1.96			1.87	1.91	1.87	1.85	2.03	1.99
Fe^{3+}	0.06			-	-	-	-	0.01	-
Mn^{2+}	-			-	-	<0.01	<0.01	-	-
Fe^{2+}	-			<0.01	-	0.01	<0.01	-	-
Sum T1	2.02			1.87	1.92	1.88	1.86	2.04	1.99
Si^{4+}	1.98			2.06	2.05	2.07	2.09	1.98	2.03
Sum T2	1.98			2.06	2.05	2.07	2.09	1.98	2.03

Footnotes: S.D. = 1σ standard deviation; *n* – number of analyses; n.d. – not detected; [1] – present study; [2] – Moro *et al.* (2001); [3] – Fortey and Beddoe-Stephens (1982); [a-f] – sample numbers: [a] – PB–6I; [b] – IF–13; [c] – PB–1; [d] – PB–6F; [e] – CRZ3552E (analysis # 1); [f] – BH2 (analysis # 8).

https://doi.org/10.1180/mgm.2022.62 Published online by Cambridge University Press

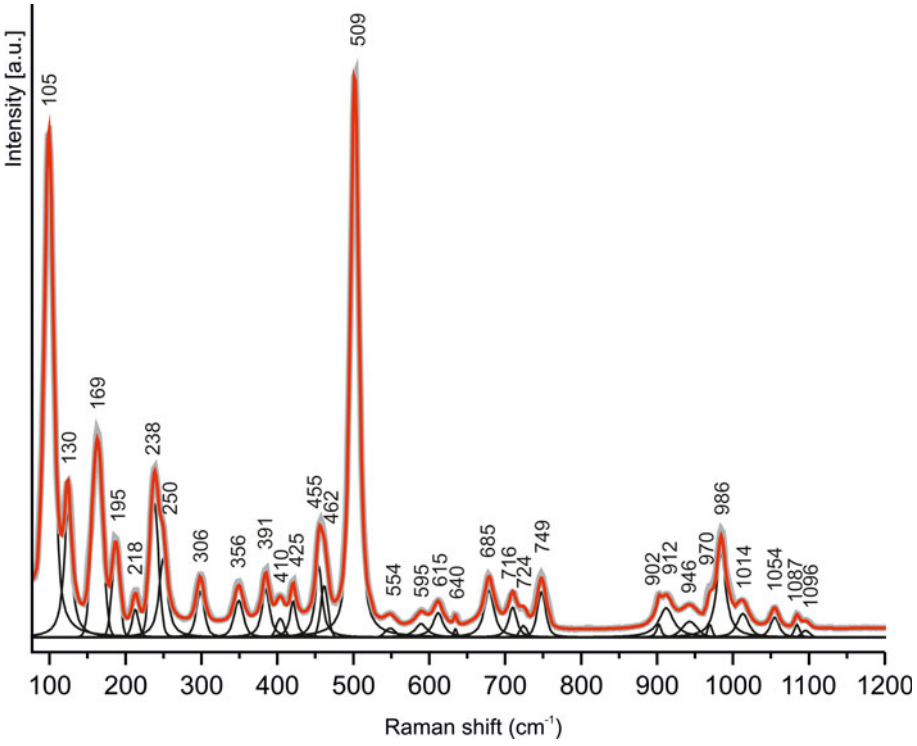

Fig. 9. Raman spectrum of celsian from Caspar quarry, Bellerberg volcano, Germany.

615, 640, 685, 716, 724 and 749 cm^{-1}. Lastly, group V is 900–1200 cm^{-1}, with nine characteristic bands in the celsian spectrum (Fig. 9). This spectral region is related to the breathing modes of tetrahedra, including T–O stretching vibrations (McKeown, 2005; Freeman *et al.*, 2008). Raman bands above 1200 cm^{-1} were not detected in the spectrum of celsian from the Caspar quarry locality.

The slight differences observed in the band placement in the celsian Raman spectrum compared to the ranges of other feldspar minerals, e.g. albite, orthoclase, or microcline, are related to the chemical composition and the presence of monovalent (K^+, Na^+) and divalent (Ba^{2+}) ions in the crystal structure of these phases (Freeman *et al.*, 2008). Raman spectroscopic analyses of Ba-rich K-feldspar from the black shale sequence in Anhui Province, South China (Chang *et al.*, 2018) proved that the strongest bands in the Ba-rich K-feldspar Raman spectrum are shifted slightly to the higher wavenumbers towards celsian frequencies.

Genetic aspect

The wide variety of minerals in the xenoliths occurring within the volcanic rocks of the Bellerberg area is due to a distinct protolith composition and subsequent metamorphic transformation (Hentschel, 1987; Mihajlovic *et al.*, 2004; Juroszek *et al.*, 2018).

The mineral assemblages detected in the samples studied are primarily products of the high-temperature transformation of argillaceous limestone xenoliths within basalt magma, in a temperature not lower than 1060°C, $X_{CO_3} < 0.55$ at $P_{total} = 1$ Kbar (Grapes, 2006; Juroszek *et al.*, 2018). High-temperature pyrometamorphic processes of limestone xenolith transformation at the sanidinite facies have predominantly isochemical character and are similar to the cement clinker production process. The initial composition of xenoliths determines the possibility of an insignificant amount of silica melt appearance both on the xenolith surface and inside it (Whitley *et al.*, 2020). In natural clinkerisation processes, wollastonite, larnite, gehlenite, magnesioferrite, brownmillerite and minerals of the shulamitite–sharyginite series form. In addition, chlormayenite or fluorapatite may also appear in the presence of volatile components. Analogous crystallisation conditions have been estimated for some clinker-like pyrometamorphic rocks and paralavas with similar mineral assemblages from the Hatrurim Complex in Israel (Vapnik *et al.*, 2007; Novikov *et al.*, 2013; Galuskina *et al.*, 2017b). There is no zonation characteristic for skarns forming with participation of fluids in the studied xenoliths. The heterogeneous distribution of high-temperature mineral association in the altered xenoliths is defined mainly by their primary heterogeneity and mineral crystallisation sequence. During contact of carbonate-rich rock (xenolith) with magma, a significant reduction of mechanical integrity takes place, together with a dynamic element exchange. More common elements, such as Ca, are incorporated into the structures of high-temperature rock-forming minerals, while more incompatible elements that are distributed within the limestone protolith, such as Ba, Sr, or Ti, remain in the melt. Moreover, crystallisation of calcium silicates at the temperature peak of pyrometamorphism determines the Ba and Sr concentration in intergranular spaces filled with a liquid phase, probably, with silicate melt enriched in Na and locally in Al, P and Ti. From this residual melt, xenomorphic crystals of bennesherite, fresnoite, walstromite, celsian and zadovite grains form together with nepheline, usually between large wollastonite crystals. Such an occurrence, and the small size of Ba and Sr-bearing minerals, indicate their later formation at temperatures below 1000°C. Slightly lowering the temperature is related to the increasing alkali components, which are embedded into the structure of nephelines and melilite-group minerals. A similar mechanism of bennesherite, fresnoite, walstromite, celsian, hexacelsian and zadovite formation from the residual melt in rankinite paralava has been described previously in pyrometamorphic rocks of the Hatrurim Complex (Krzątała *et al.*, 2022).

The diversity of accessory minerals identified in xenolith samples from the Bellerberg volcano is reflected in formation conditions

https://doi.org/10.1180/mgm.2022.62 Published online by Cambridge University Press

such as temperature, transformation during metamorphism, and the availability of suitable components. In samples analysed, both ferric- and ferrous-bearing accessory phases were distinguished. Brownmillerite and minerals belonging to the shulamitite–sharyginite series in which all iron is as Fe^{3+} indicated crystallisation at a temperature of ~1000°C (Juroszek *et al.*, 2018). In turn, ferrous melilites, such as bennesherite, Fe^{2+}-åkermanite, or Sr-bennesherite, as described above, crystallised later from the residual melt and in lower-temperature conditions, below 1000°C. The general decrease in oxygen activity may be related to the mass crystallisation of rock-forming minerals in the xenolith, mainly Ca-silicates and other high-temperature oxide minerals. Small portions of the residual melt in-between earlier crystallised phases were enriched in non-compatible elements, such as Ba and Sr, hence heterovalent iron was probably incorporated into the bennesherite and other melilite structures as Fe^{2+}. Moreover, the crystal chemistry features of such mineral phases determine the stabilisation of ferrous iron, which was also confirmed by the structural analyses of bennesherite detected in rankinite paralava of the Hatruim Complex (Krzątała *et al.*, 2022).

Conclusions

The results obtained in the present work suggest the following conclusions.

Carbonate–silicate xenoliths embedded in alkali basalt from Caspar quarry in the Bellerberg volcano still deserve attention as a source of unique minerals, as evidenced by rare Ba-bearing minerals, including bennesherite, fresnoite, walstromite and celsian being recognised and described for the first time in this locality.

The diversity observed in the chemical composition of various melilite-group minerals and significant substitution at the X and T1 positions indicate the presence of potentially new minerals within this group, such as Sr-bennesherite or ferrous-bearing åkermanite, identified in this work in xenolith samples.

The presence of the P-analogue of gurimite, as a tiny inclusion in bennesherite, has allowed us to confirm the additional occurrence of this new mineral, known already as mazorite, $Ba_3(PO_4)_2$, and recently approved by the CNMNC IMA (IMA2022–022, Juroszek *et al.*, 2022).

Detailed Raman analyses performed for bennesherite confirm the decreasing band frequencies due to the predominance of the Ba atom at the X position. It implies that the Raman spectroscopy method might be used, at least partially, as an effective tool to distinguish various melilite-group members.

A similar mineral association and scheme of crystallisation observed in xenoliths from Caspar quarry and paralava samples from the Hatrurim Complex show the relation between these two stratigraphical distinct geological units. The similarities observed in the micro-scale can be utilised for research in the broader context.

Acknowledgements. We thank Marlina Elburg for sharing the chemical data of bennesherite from Nyiragongo volcano and two anonymous reviewers for their helpful and constructive comments, which allowed us to improve a previous version of the manuscript.

Competing interests. The authors declare none.

References

Alfors J.T., Stinson M.C., Matthews R.A. and Pabst A. (1965) Seven new barium minerals from eastern Fresno County, California. *American Mineralogist*, **50**, 314–340.

Allu A.R., Balaji S., Tulyaganov D.U., Mather G.C., Margit F., Pascual M.J., Siegel R., Milius W., Senker J., Agarkov D.A., Kharton V.V. and Ferreira J.M.F. (2017) Understanding the formation of $CaAl_2Si_2O_8$ in melilite-based glass-ceramics: combined diffraction and spectroscopic studies. *ACS Omega*, **2**, 6233–6243.

Andersen T., Elburg M.A. and Erambert M. (2014) Extreme peralkalinity in delhayelite- and andremeyerite-bearing nephelinite from Nyiragongo volcano, East African Rift. *Lithos*, **206–207**, 164–178.

Ardit M., Cruciani G. and Dondi M. (2010) The crystal structure of Sr-hardystonite, $Sr_2ZnSi_2O_7$. *Zeitschrift für Kristallographie*, **225**, 298–301.

Ardit M., Dondi M., Merlini M. and Cruciani G. (2012) Melilite-type and melilite-related compounds: structural variations along the join $Sr_{2-x}Ba_xMgSi_2O_7$ ($0 \le x \le 2$) and high-pressure behavior of the two end-members. *Physics and Chemistry of Minerals*, **39**, 199–211.

Bindi L., Bonazzi P. and Fitton J.G. (2001) Crystal chemistry of strontian soda melilite from nephelinite lava of Mt. Etinde, Cameroon. *European Journal of Mineralogy*, **13**, 121–125.

Bouhifd M.A., Gruener G., Mysen B.O. and Richet P. (2002) Premelting and calcium mobility in gehlenite ($Ca_2Al_2SiO_7$) and pseudowollastonite ($CaSiO_3$). *Physics and Chemistry of Minerals*, **29**, 655–662.

Bychkov A., Borisov A., Kharamov D., Guzhova A.V. and Urusov V. (1992) Change of the valent and structural state of iron ions upon melting of barium ferroäkermanite $Ba_2FeSi_2O_7$. *Doklady Akademii Nauk SSSR*, **322**, 525–530.

Chang C., Hu W.-X., Fu Q., Cao J., Wang X.-L., Wan Y. and Yao S.-P. (2018) Characteristics and formation processes of (Ba,K,NH_4)-feldspar and cymrite from a lower Cambrian black shale sequence in Anhui Province, South China. *Mineralogical Magazine*, **82**, 1–21.

Chukanov N.V., Rastsvetaeva R.K., Britvin S.N., Virus A.A., Belakovskiy D.I., Pekov I.V., Aksenov S.M. and Ternes B. (2011) Schüllerite, $Ba_2Na(Mn,Ca)(Fe^{3+},Mg,Fe^{2+})_2Ti_2(Si_2O_7)_2(O,F)_4$, a new mineral species from the Eifel volcanic district, Germany. *Geology of Ore Deposits*, **53**, 767–774.

Coats J.S., Smith C.G., Fortey N.J., Gallagher M.J., May F. and McCourt W.J. (1980) Strata-bound barium-zinc mineralization in Dalradian schist near Aberfeldy, Scotland. *Institution of Mining and Metallurgy, Transactions, Section B*, **89**, 110–122.

Dai Y., Zhu B., Qiu J., Ma H., Lu B., Cao S. and Yu B. (2007) Direct writing three-dimensional $Ba_2TiSi_2O_8$ crystalline pattern in glass with ultrashort pulse laser. *Applied Physics Letters*, **90**, 181109.

Dowty E. (1987) Vibrational interactions of tetrahedra in silicate glasses and crystals. *Physics and Chemistry of Minerals*, **14**, 80–93.

Dunning G. (2018) Barium silicate mineralogy of the Western Margin, North America continent, Part 1: Photographic documentation of barium silicates and associated minerals from Baja California Norte, Mexico, Western Canada and Alaska, USA. *Baymin Journal*, **19**, 1–87.

Dunning G.E. and Cooper J.F.J. (1999) Barium silicate minerals from Trumbull Peak, Mariposa County, California. *The Mineralogical Record*, **30**, 411–417.

Dunning G. and Walstrom R. (2018) Barium silicate mineralogy of the Western Margin, North America continent, Part 1: Geology, origin, paragenesis and mineral distribution from Baja California Norte, Mexico, Western Canada and Alaska, USA. *Baymin Journal*, **19**, 1–70.

Fortey N.J. and Beddoe-Stephens B. (1982) Barium silicates in stratabound Ba-Zn mineralization in the Scottish Dalradian. *Mineralogical Magazine*, **46**, 63–72.

Freeman J.J., Wang A., Kuebler K.E., Jolliff B.L. and Haskin L.A. (2008) Characterization of natural feldspars by Raman spectroscopy for future planetary exploration. *The Canadian Mineralogist*, **46**, 1477–1500.

Gabelica-Robert M. and Tarte P. (1981) Vibrational spectrum of fresnoite ($Ba_2TiOSi_2O_7$) and isostructural compounds. *Physics and Chemistry of Minerals*, **7**, 26–30.

Gaft M., Yeates H. and Nagli L. (2013) Laser-induced time-resolved luminescence of natural margarosanite $Pb(Ca,Mn)_2Si_3O_9$, swedenborgite $NaBe_4SbO_7$ and walstromite $BaCa_2Si_3O_9$. *European Journal of Mineralogy*, **25**, 71–77.

Galuskin E.V., Gfeller F., Galuskina I.O., Pakhomova A., Armbruster T., Vapnik Y., Włodyka R., Dzierżanowski P. and Murashko M. (2015) New minerals with a modular structure derived from hatrurite from the pyrometamorphic Hatrurim Complex. Part II. Zadovite, $BaCa_6[(SiO_4)(PO_4)]$

https://doi.org/10.1180/mgm.2022.62 Published online by Cambridge University Press

$(PO_4)_2F$ and aradite, $BaCa_6[(SiO_4)(VO_4)](VO_4)_2F$, from paralavas of the Hatrurim Basin, Negev Desert, Israel. *Mineralogical Magazine*, **79**, 1073–1087.

Galuskin E.V., Krüger B., Krüger H., Blass G., Widmer R. and Galuskina I.O. (2016) Wernerkrauseite, $CaFe^{3+}_2Mn^{4+}O_6$: the first nonstoichiometric post-spinel mineral, from Bellerberg volcano, Eifel, Germany. *European Journal of Mineralogy*, **28**, 485–493.

Galuskina I.O., Galuskin E.V., Vapnik Y., Prusik K., Stasiak M., Dzierżanowski P. and Murashko M. (2017a) Gurimite, $Ba_3(VO_4)_2$ and hexacelsian, $BaAl_2Si_2O_8$ – two new minerals from schorlomite-rich paralava of the Hatrurim Complex, Negev Desert, Israel. *Mineralogical Magazine*, **81**, 1009–1019.

Galuskina I.O., Galuskin E.V., Pakhomova A.S., Widmer R., Armbruster T., Krüger B., Grew E.S., Vapnik Y., Dzierażanowski P. and Murashko M. (2017b) Khesinite, $Ca_4Mg_2Fe^{3+}_{10}O_4[(Fe^{3+}_{10}Si_2)O_{36}]$, a new rhönite-group (sapphirine supergroup) mineral from the Negev Desert, Israel – natural analogue of the SFCA phase. *European Journal of Mineralogy*, **29**, 101–116.

Grapes R.H. (2006) *Pyrometamorphism*. Springer, Heidelberg, Berlin [Chapter: Calc-silicates and evaporates, pp. 115–166].

Grice J.D., Kristiansen R., Friis H., Rowe R., Cooper M.A., Poirier G.G., Yang P. and Weller M.T. (2017) Hydroxylgugiaite: a new beryllium silicate mineral from the Larvik Plutonic Complex, Southern Norway and the IlÍmaussaq Alkaline Complex, South Greenland; the first member of the melilite group to incorporate a hydrogen atom. *The Canadian Mineralogist*, **55**, 219–232.

Hanuza J., Ptak M., Mączka M., Hermanowicz K., Lorenc J. and Kaminskii A.A. (2012) Polarized IR and Raman spectra of $Ca_2MgSi_2O_7$, $Ca_2ZnSi_2O_7$ and $Sr_2MgSi_2O_7$ single crystals: Temperature-dependent studies of commensurate to incommensurate and incommensurate to normal phase transitions. *Journal of Solid State Chemistry*, **191**, 90–101.

Hentschel G. (1987) *Die Mineralien der Eifelvulkane*. 2nd edition. Weise Verlag, München, Germany.

Holtstam D., Cámara F. and Karlsson A. (2021) Instalment of the margarosanite group, and data on walstromite–margarosanite solid solutions from the Jakobsberg Mn–Fe deposit, Värmland, Sweden. *Mineralogical Magazine*, **85**, 224–232.

Juroszek R., Krüger H., Galuskina I., Krüger B., Jeżak L., Ternes B., Wojdyla J., Krzykawski T., Pautov L. and Galuskin E. (2018) Sharyginite, $Ca_3TiFe_2O_8$, A new mineral from the Bellerberg Volcano, Germany. *Minerals*, **8**, 308.

Juroszek R., Galuskina I.O., Krüger B., Krüger H., Vapnik Y. and Galuskin E. (2022) Mazorite, IMA 2022-022. CNMNC Newsletter 68. *Mineralogical Magazine*, **86**, doi:10.1180/mgm.2022.93.

Kimata M. (1983) The structural properties of synthetic Sr-åkermanite, $Sr_2MgSi_2O_7$. *Zeitschrift für Kristallographie – Crystalline Materials*, **163**, 295–304.

Kimata M. (1984) The structural properties of synthetic Sr-gehlenite, $Sr_2Al_2SiO_7$. *Zeitschrift für Kristallographie*, **167**, 103–116.

Krzątała A., Krüger B., Galuskina I., Vapnik Y. and Galuskin E. (2020) Walstromite, $BaCa_2(Si_3O_9)$, from Rankinite Paralava within Gehlenite Hornfels of the Hatrurim Basin, Negev Desert, Israel. *Minerals*, **10**, 407.

Krzątała A., Krüger B., Galuskina I., Vapnik Y. and Galuskin E. (2022) Bennesherite, $Ba_2Fe^{2+}Si_2O_7$: A new melilite group mineral from the Hatrurim Basin, Negev Desert, Israel. *American Mineralogist*, **107**, 138–146.

Louisnathan S.J. (1971) Refinement of the crystal structure of a natural gehlenite, $Ca_2Al(Al,Si)_2O_7$. *The Canadian Mineralogist*, **10**, 822–837.

Marincea S., Dumitras D.-G., Ghinet C., Fransolet A.-M., Hatert F. and Rondeaux M. (2011) Gehlenite from three occurrences of high-temperature skarns, Romania: New mineralogical data. *The Canadian Mineralogist*, **49**, 1001–1014.

Markgraf S.A., Sharma S.K. and Bhalla A.S. (1992) Raman study of glasses of $Ba_2TiSi_2O_8$ and $Ba_2TiGe_2O_8$. *Journal of the American Ceramic Society*, **75**, 2630–2632.

Matsubara S., Ritsuro M., Kato A., Yokoyama K. and Okamoto A. (1998) Okayamalite, $Ca_2B_2SiO_7$, a new mineral, boron analogue of gehlenite. *Mineralogical Magazine*, **62**, 703–706.

McKeown D.A. (2005) Raman spectroscopy and vibrational analyses of albite: From 25°C through the melting temperature. *American Mineralogist*, **90**, 1506–1517.

Mihajlovic T., Lengauer C.L., Ntaflos T., Kolitsch U. and Tillmanns E. (2004) Two new minerals rondorfite, $Ca_8Mg[SiO_4]_4Cl_2$, and almarudite, $K(\square, Na)_2(Mn,Fe,Mg)_2(Be,Al)_3[Si_{12}O_{30}]$, and a study of iron-rich wadalite, $Ca_{12}[(Al_8Si_4Fe_2)O_{32}]Cl_6$, from the Bellerberg (Bellberg) volcano, Eifel, Germany. *Neues Jahrbuch für Mineralogie – Abhandlungen*, 265–294.

Moro M.C., Cembranos M.L. and Fernandez A. (2001) Celsian, (Ba, K)-feldspar and cymrite from Sedex barite deposits of Zamora, Spain. *The Canadian Mineralogist*, **39**, 1039–1051.

Novikov I., Vapnik Y. and Safonova I. (2013) Mud volcano origin of the Mottled Zone, South Levant. *Geoscience Frontiers*, **4**, 597–619.

Ogorodova L.P., Gritsenko Y.D., Vigasina M.F., Bychkov A.Y., Ksenofontov D.A. and Melchakova L.V. (2018) Thermodynamic properties of natural melilites. *American Mineralogist*, **103**, 1945–1952.

Peng C.J., Tsao R.L. and Chou Z.R. (1962) Gugiaite, $Ca_2BeSi_2O_7$, a new beryllium mineral and its relation to the melilite group. *Scientia Sinica*, **11**, 977–988.

Peretyazhko I.S., Savina E.A., Khromova E.A., Karmanov N.S. and Ivanov A.V. (2018) Unique clinkers and paralavas from a new Nyalga combustion metamorphic complex in Central Mongolia: Mineralogy, geochemistry, and genesis. *Petrology*, **26**, 181–211.

Richet P., Mysen B.O. and Ingrin J. (1998) High-temperature X-ray diffraction and Raman spectroscopy of diopside and pseudowollastonite. *Physics and Chemistry of Minerals*, **6**, 401–414.

Sharma S.K., Simons B. and Yoder H.S. (1983) Raman study of anorthite, calcium Tschermak's pyroxene, and gehlenite in crystalline and glassy states. *American Mineralogist*, **68**, 1113–1125.

Sharma S.K., Yoder H.S. and Matson D.W. (1988) Raman study of some melilites in crystalline and glassy states. *Geochimica et Cosmochimica Acta*, **52**, 1961–1967.

Sitarz M., Mozgawa W. and Handke M. (1997) Vibrational spectra of complex ring silicate anions — method of recognition. *Journal of Molecular Structure*, **404**, 193–197.

Sjögren H. (1895) Celsian, en anorthiten motsvarande bariumfältspat från Jakobsberg. Preliminärt meddelande. *Geologiska Föreningens i Stockholm Förhandlingar*, **17**, 578–582.

Solovova I.P., Girnis A.V., Ryabchikov I.D. and Kononkova N.N. (2009) Mechanisms of formation of barium-rich phlogopite and strontium-rich apatite during the final stages of alkaline magma evolution. *Geochemistry International*, **47**, 578–591.

Spencer L.J. (1942) Barium-felspars (celsian and paracelsian) from Wales. *Mineralogical Magazine and Journal of the Mineralogical Society*, **26**, 231–245.

Środek D., Juroszek R., Krüger H., Krüger B., Galuskina I. and Gazeev V. (2018) New occurrence of rusinovite, $Ca_{10}(Si_2O_7)_3Cl_2$: composition, structure and Raman data of rusinovite from Shadil-Khokh Volcano, South Ossetia and Bellerberg Volcano, Germany. *Minerals*, **8**, 399.

Swainson I.P., Dove M.T., Schmahl W.W. and Putnis A. (1992) Neutron powder diffraction study of the åkermanite–gehlenite solid solution series. *Physics and Chemistry of Minerals*, **19**, 185–195.

Vapnik Y., Sharygin V.V., Sokol E.V. and Shagam R. (2007) Paralavas in a combustion metamorphic complex: Hatrurim Basin, Israel. In: *Geology of Coal Fires: Case Studies from Around the World* (G.B. Stracher, editor). Geological Society of America, Boulder, Colorado, USA.

Whitley S., Halama R., Gertisser R., Preece K., Deegan F.M. and Troll V.R. (2020) Magmatic and metasomatic effects of magma–carbonate interaction recorded in calc-silicate xenoliths from Merapi volcano (Indonesia). *Journal of Petrology*, **61**, 1–38.

Wiedenmann D., Zaitsev A.N., Britvin S.N., Krivovichev S.V. and Keller J. (2009) Alumoåkermanite, $(Ca,Na)_2(Al,Mg,Fe^{2+})(Si_2O_7)$, a new mineral from the active carbonatite–nephelinites–phonolite volcano Oldoinyo Lengai, northern Tanzania. *Mineralogical Magazine*, **73**, 373–384.

Wolff J.E. (1899) On hardystonite, a new calcium-zinc silicate from Franklin Furnace, New Jersey. *Proceedings of the American Academy of Arts and Sciences*, **34**, 479–481.

Yadav A.K. and Singh P. (2015) A review of the structures of oxide glasses by Raman spectroscopy. *RSC Advances*, **5**, 67583–67609.

Zhu B., Dai Y., Ma H., Zhang S., Lin G. and Qiu J. (2007) Femtosecond laser induced space-selective precipitation of nonlinear optical crystals in rare-earth-doped glasses. *Optics Express*, **15**, 6069–6074.

https://doi.org/10.1180/mgm.2022.62 Published online by Cambridge University Press